Diverse toxins exhibit a common binding mode to the Nicotinic Acetylcholine Receptors

Hung N. Do[1], Jessica Z. Kubicek-Sutherland[2], S. Gnanakaran[1,*]

[1]Theoretical Biology and Biophysics Group, Theoretical Division; and [2]Physical Chemistry and Applied Spectroscopy Group, Chemistry Division, Los Alamos National Laboratory, Los Alamos, New Mexico 87545, USA

[*]Correspondence: gnana@lanl.gov

Abstract

Nicotinic acetylcholine receptors (nAChRs) are critical ligand-gated ion channels in the human nervous system. They are targets for various neurotoxins produced by algae, plants, and animals. While many structures of nAChRs bound by neurotoxins have been published, the binding mechanism of toxins to the nAChRs remains unclear. In this work, we have performed extensive Gaussian accelerated molecular dynamics simulations on several *Aplysia californica* (AC) nAChRs in complex with α-conotoxins, strychnine, and pinnatoxins, as well as human nAChRs in complex with α-bungarotoxin and α-conotoxin to determine the binding and dissociation pathways of the toxins to the nAChRs and the associated effects. We uncovered two common binding and dissociation pathways shared by toxins and nAChRs. In the first binding pathway, the toxins diffused from the bulk solvent to bind a region near the extracellular pore before moving downwards along the nAChRs to the nAChR orthosteric pocket. The second binding pathway involved a direct diffusion of the toxins from the bulk solvent into the nAChR orthosteric pocket. The dissociation pathways were the reverse of the observed binding pathways. Notably, we determined that the electrostatically bipolar interactions between nAChR orthosteric pocket and toxins provided an explanation for the common binding mode shared by diverse toxins.

Statement of Significance

We have performed extensive Gaussian accelerated molecular dynamics simulations on several nAChRs in complex with α-conotoxins, strychnine, pinnatoxins, and α-bungarotoxin. We uncovered two common binding and dissociation pathways shared by toxins and nAChRs. In the first pathway, the toxins diffused from the bulk solvent to bind a region near the extracellular pore before moving downwards along the nAChRs to the nAChR orthosteric pocket. The second pathway involved a direct diffusion of the toxins from the bulk solvent into the nAChR orthosteric pocket. Notably, we determined that the electrostatically bipolar interactions between nAChR orthosteric pocket and toxins served as the explanation for the common binding mode shared by diverse toxins.

Introduction

Nicotinic acetylcholine receptors (nAChRs) are critical ligand-gated ion channels in the human nervous system, which can be divided into two groups, including muscle receptors and neuronal receptors, and targets for various neurotoxins produced by algae, plants, and animals[1,2]. nAChRs are pentameric (five subunits) proteins that can be composed of homomeric subunits (all of the same type, such as α7, α8, and α9) and heteromeric subunits (with multiple subunits combined from the combinations of α2-α6 with β2-β4, α9 with α10, or α1 with β1, δ, and γ or ε), resulting in diverse functional properties[1,3]. A total of seventeen different nAChR subunits have been identified, including α1-α10, β1-β4, δ, γ and ε[1]. The subunits are structurally similar but diverse in sequences[3], thus displaying varying binding interactions and affinities towards different toxins[4].

nAChRs are allosteric proteins, with a complete nAChR structure consisting of the extracellular ligand binding domain, a bundle of transmembrane helices, and a cytoplastic C-terminal latch that was shown to modulate channel opening[2,5]. The gating mechanism of nAChRs has been shown to consist of three primary states, including the resting, activated, and desensitized state[5]. In the resting state, an antagonist binds to the nAChR, resulting in the closure of the cationic channel of the receptor[5]. In the activated state, an agonist binds to the ligand binding pocket of the nAChR, opening the cationic channel and making the receptor highly permeable to cations[5]. The desensitized state could be considered the intermediate state between the resting and activated state, as the cationic channel of nAhCR closes to ion permeation despite the binding of an agonist[5]. Protein toxins produced by marine snails (α-conotoxins) and snakes (α-bungarotoxins) have been shown to display especially high affinity (**Table 1**) and selectivity for nAChRs[6].

Conotoxins are a family of extremely toxic neurotoxins composed of cysteine-rich peptides produced by marine cone snails[7-9]. They are small 13-15 amino acid peptide toxins that act as competitive inhibitors of nAChRs binding to the acetylcholine ligand binding site located between subunits[10]. The natural conotoxin sequences are incredibly diverse[11]. It is estimated that less than two percent of existing conotoxins have been sequenced[12]. Over the last two decades, many X-ray crystal structures of α-conotoxins bound to the soluble

acetylcholine binding protein (AChBP), a structural homolog of nAChR containing the ligand binding extracellular domain, have been published[10]. α-Bungarotoxin is a relatively large 74 amino acid peptide toxin found in the venom of certain snakes[13]. It has been shown to irreversibly bind to the human α7 nAChR subunit[14], with a cryo-EM structure published[5]. Strychnine is a highly potent alkaloid (non-protein) neurotoxin produced by poisonous plants that has been shown to inhibit muscle and neuronal nAChRs[15]. A X-ray crystal structure of strychnine in complex with AChBP has been published[16]. Pinnatoxin is a macrocyclic imine (non-protein) marine phycotoxin produced by algae with high affinity for α7 and $\alpha 1_2\beta\gamma\delta$ nAChRs[17] (**Table 1**). X-ray crystal structures of pinnatoxin A and pinnatoxin G in complex with AChBP have been published[17].

Molecular dynamics (MD) is a compelling computational technique for simulating biomolecular dynamics on an atomistic level[18] and can lead to the understanding of binding modes. MD simulation have been used in various studies to explore the binding and interactions between toxins, specifically α-conotoxins, and nAChRs[19]. In particular, Beissner et al. applied MD simulations to calculate binding enthalpies to show that charge was the most important feature in the selectivity of α-conotoxins towards the α3β2 over the α4β2 nAChR subtype[19,20]. Yu et al. employed computational scan and binding free energy calculations of single point mutants to show that dispersion plus desolvation forces and electrostatic forces controlled the binding affinity and selectivity of the ImI α-conotoxin towards the α7 nAChR, respectively[19,21]. Cuny et al. performed MD simulations and revealed that receptor side chain length was responsible for the binding affinities of α-RegIIA for the α3β2 and α3β4 nAChRs[19,22]. Pucci et al. combined MD simulations with docking to determine the important interactions between the N-terminal tripeptide tail of the α-PIA conotoxin with the α6β2 nAChR[19,23]. Furthermore, Yu et al. used a combination of MD simulations and calculations of binding free energy to identify the binding site of α-conotoxin Vc1.1 to the α9α10 nAChR, which was confirmed by experiment[19,24]. Suresh and Hung performed umbrella sampling MD simulations to examine the binding of α-conotoxin [Y4E]GID with the α4β2 and α7 nAChR[19,25]. Meanwhile, Yu et al. used random accelerated

molecular dynamics and steered molecular dynamics to explore multiple unbinding pathways of the α-conotoxin ImI from the α7 nAChR[19,26].

Gaussian accelerated molecular dynamics (GaMD) is another enhanced sampling MD technique that can be used to explore toxin binding and dissociation from the nAChR[27]. GaMD is an unconstrained (i.e., collective-variable-independent) enhanced sampling technique that facilitates dynamic transitions by applying a harmonic boost potential to smooth the biomolecular potential energy surface[27]. Since the boost potential usually exhibits a near Gaussian distribution, GaMD can maintain the overall shape of the original free energy surface, and cumulant expansion to the second order ("Gaussian approximation") can be applied to achieve proper energy reweighting[27]. GaMD has been demonstrated to properly sample the biological processes of ligand binding[28] and protein conformational changes upon ligand binding[29].

In this work, we want to examine whether a diverse set of toxins (α-conotoxins, strychnine, and pinnatoxins) (**Figure 1**) share a common binding mode regardless of the origin (human or sea organism) or the different constructs (soluble surrogate and the fully membrane-bound) of nAChR. We performed GaMD simulations on a number of *Aplysia californica* (AC) nAChRs in complex with α-conotoxins, strychnine, and pinnatoxins, as well as human membrane-bound nAChRs in complex with α-bungarotoxin and α-conotoxin (**Figures 2** and **S1**) to determine the binding and dissociation pathways of the toxins to the nAChRs as well as the associated effects. We deduce the common binding mode shared across multiple ligands in the nAChRs. Our work provides important mechanistic insights into the binding of toxins in the nAChRs and identifies the key binding descriptors involved in the process.

Methods

Simulation system setup

We started from the X-ray crystal structures of *Aplysia californica* (AC) nAChR in apo state and in complex with α-conotoxin BuIA, α-conotoxin ImI, α-conotoxin RgIA, strychnine, pinnatoxin A, and pinnatoxin G, and the cryo-EM structures of human α7 nAChR in apo state

and in complex with α-bungarotoxin to prepare the simulation systems (**Table 2** and **Figures 1-2**). The missing residues within the structures were restored using the SWISS-MODEL homology modeling webserver[30] (**Table 3**). The starting structures of the AC nAChR and human α7-nAChR with free α-conotoxin RgIA were prepared by removing the orthosteric ligands (if present) from the nAChR orthosteric pockets and placing five RgIA molecules ~20 Å away from the receptors extracellularly (**Table 2** and **Figure S1**). The CHARMM-GUI webserver[31-33] was used to prepare the simulation systems. All heteroatom molecules, except the toxins, were removed from the starting structures. The protein chain termini were capped with neutral patches (acetyl and methylamide), except the C-terminal of the α-conotoxin BuIA, where amide was used to be consistent with the 4EZ1[34] PDB structure. The starting structures of AC nAChR simulation systems were solvated in 0.15 M NaCl solution boxes that extended ~10 Å from the solute surfaces. The structures of human nAChR simulation systems were embedded in POPC membrane lipid bilayers and then solvated in 0.15 M NaCl solutions. The AMBER[35] force field parameter sets were used for the GaMD simulations, including the ff14SB[36] for proteins, GAFF2[37] for ligands using the AM1-BCC[38] charging method, LIPID17 for lipids, and TIP3P[39] for water.

Simulation protocols

All-atom dual-boost GaMD simulations[27] were performed on the nAChR simulation systems to examine the binding and dissociation of the toxins to the receptors. We used the standard builds of the simulation software AMBER 22[40] according to the best practices for running GaMD[27] simulations. Periodic boundary conditions were applied to the simulation systems, and bonds containing hydrogen atoms were restrained with the SHAKE[41] algorithm. A timestep of 2 fs was used. The temperature was kept constant at 310 K using the Langevin thermostat[42,43] with a friction coefficient of 1.0 ps^{-1}. The electrostatic interactions were calculated using the particle mesh Ewald (PME) summation[44] with a cutoff of 9.0 Å for long-range interactions. The pressure was kept constant at 1.0 bar using the Berendsen barostat[45,46] with isotropic coupling for the soluble AC nAChR simulation systems and with semi-isotropic coupling for the membrane-bound human nAChR simulation systems,

respectively. The Berendsen coupling constant was set to 0.5 ps. The GPU version of the *pmemd* module (*pmemd.cuda*) in AMBER 22[40] was used to carry out the MD simulations of nAChRs. We used the default input files produced by the CHARMM-GUI webserver[31-33] to carry out the initial energetic minimization, equilibration, and cMD simulations for all simulation systems. The simulation systems were energetically minimized for 5000 steps using the steepest-descent algorithm and equilibrated with the constant number, volume, and temperature (NVT) ensemble. The membrane-bound human nAChR systems were further equilibrated with the constant number, pressure, and temperature (NPT) ensemble. The conventional MD (cMD) simulations were then performed for 10 ns using the NPT ensemble. GaMD simulations of the soluble AC nAChR systems involved an initial short cMD simulation of 4-10 ns to calculate GaMD acceleration parameters, followed by the GaMD equilibration stage of 16-40 ns to equilibrate and update the acceleration parameters. On the other hand, GaMD simulations of the membrane-bound human nAChR systems consisted of an initial short cMD simulation of 8-10 ns and GaMD equilibration simulation of 32-40 ns. Five independent 1000 ns GaMD production simulations with randomized initial atomic velocities and acceleration parameters kept constant were performed for each nAChR system. The dual-boost scheme was used, with one boost potential applied to the dihedral energetic term and another to the total potential energetic term. The reference energy E was set to lower bound ($E = V_{max}$) for both dihedral and total potential energy. The upper limits of the boost potential standard deviations, σ_0, were set to 6.0 kcal/mol for both the dihedral (σ_{0D}) and total (σ_{0P}) potential energetic terms. The GaMD simulations are summarized in **Table 2**.

Simulation analysis

The AmberTools20[47,48], along with their associated scripts, were used to analyze the simulation trajectories. The PyReweighting[49] toolkit was used to calculate the two-dimensional (2D) free energy profiles. We considered three different reaction coordinates relevant to the association/dissociation of toxins to the nAChR (**Figure S2**). The first coordinate tracked the center-of-mass (COM) distance between the toxin and the

orthosteric pocket. The second coordinate tracked the opening and closing of the loop at the orthosteric pocket to capture its influence on trapping toxins. The third coordinate provided an estimation of the diameter of the nAChR extracellular pore. Here, the first coordinate was the distance between the COM of the toxin and the orthosteric pocket which was defined based on the residues Q186 to Y195 within a single subunit. On the toxin side, for strychnine, all heavy atoms were considered, whereas for RgIA, only the Cα atoms of α-conotoxin RgIA were considered in the calculation of COM (**Figure S2a**). For the second coordinate, the distance between the COM of the AC-nAChR orthosteric pockets (involving residues Q186 – Y195) and the COM of residues L29 to D44 and N48 to K61 from the neighboring subunit was taken into account (**Figure S2b**). For the third coordinate, the distance between the Cα-atoms of residues A:Q100 and D:Q100 accounted for extracellular pore (**Figure S2c**). The numbering schemes of the AC nAChR was based on the 2BYP[50] PDB structure, with the chain ID listed before the colon and residue numbers included after the colons. A bin size of 1.0-2.0 Å and cutoff of 100 frames in one bin were used for reweighting of the GaMD simulations of strychnine dissociation and RgIA binding in the nAChRs. Furthermore, we considered nAChR residues within 4 Å distance of the toxins to be interacting residues. The hierarchical agglomerative clustering algorithm was used to obtain representative conformations of the low-energy conformational states observed in the binding and dissociation of toxins in the nAChRs. Given that nAChRs consisted of five different subunits with identical binding pockets, we only considered distances between toxins and AC-nAChR orthosteric pockets of ≤ 40 Å in the 2D free energy profiles to avoid identical toxin-nAChR conformational states from different subunits. We also calculated the root-mean-square fluctuations (RMSFs) and performed principal component analysis (PCA) to determine the changes in nAChR flexibility upon toxin binding and primary motions in the simulation systems, respectively, to examine the effects of toxin binding to the nAChRs. The PCA were carried out following the protocols described in the AmberTools[48,51] tutorial (https://amberhub.chpc.utah.edu/introduction-to-principal-component-analysis/). The PCA were carried out on all backbone atoms of the nAChRs for each production simulation trajectory in each simulation system. We averaged the first PCs obtained from each production simulation trajectory in each simulation system

and showed only the motions with ≥6Å distances with RMSDs of ~3Å using VMD[52] for all simulation systems in the **Supporting Information** for clarity. Lastly, we followed the following protocol to calculate the dipole moments for the toxins and ligands from their structures. We first obtained the atomic charges (in the units of electron charges, *e*) of the toxins/ligands from the simulation topology files and their respective *xyz* coordinates from their structures (in the units of *Å*). The dipole moments for each toxin/ligand were then calculated using the following formulas:

$$\vec{\mu}_{atom} = e_{atom} \cdot (x_{atom}, y_{atom}, z_{atom}) = (e_{atom}x_{atom}, e_{atom}y_{atom}, e_{atom}z_{atom}) = (\mu_{x,atom}, \mu_{y,atom}, \mu_{z,atom}) \quad (1)$$

$$\vec{\mu}_{toxin} = \left(\sum_{i=1}^{N} \mu_{x,atom}, \sum_{i=1}^{N} \mu_{y,atom}, \sum_{i=1}^{N} \mu_{z,atom}\right) = (\mu_{x,toxin}, \mu_{y,toxin}, \mu_{z,toxin}) \quad (2)$$

$$\mu_{toxin} = \sqrt{\mu_{x,toxin}^2 + \mu_{y,toxin}^2 + \mu_{z,toxin}^2}\ (e.\text{Å}) \quad (3)$$

$$\mu_{toxin} = 4.803 \cdot \mu_{toxin}\ (D) \quad (4)$$

where μ stood for the dipole moments, e stood for the charges, and x, y, z were the coordinates obtained from the structures. The calculated dipole moments for the toxins were included in **Table 4**.

Results

All-atom dual-boost GaMD simulations were performed on the apo AC nAChR, α-conotoxin-BuIA-bound AC nAChR, α-conotoxin-ImI-bound AC nAChR, α-conotoxin-RgIA-bound AC nAChR, strychnine-bound AC nAChR, pinnatoxin-A-bound nAChR, pinnatoxin-G-bound nAChR, AC nAChR with free α-conotoxin RgIA, apo human α7 nAChR, α-bungarotoxin-bound human α7 nAChR, and human α7 nAChR with free α-conotoxin RgIA (**Figures 1-2** and **S1**). The seven toxins explored in this study illustrate various physical and structural properties – three peptides (α-conotoxins BuIA, ImI, and RgIA), one protein (α-bungarotoxin), one small chemical compound (strychnine), and two large chemical compounds (pinnatoxin A and G) – as well as originate from different sources – three from sea snails (α-conotoxins BuIA, ImI, and RgIA), one from snakes (α-bungarotoxin), one from poisonous

plants (strychnine), and two from algae (pinnatoxin A and G) (**Figure 1**). In addition, the constructs of the nAChRs were also diverse: the AC nAChRs only included the soluble extracellular ligand binding domain, whereas the human α7 nAChR consisted of the soluble extracellular ligand binding domains, the transmembrane helical regions, as well as the intracellular domains (**Figures 2** and **S1**).

The boost potentials applied in the GaMD simulations of the nAChRs were recorded to be similar across the systems, with the average values of 11.8 – 14.6 kcal/mol and standard deviations of 3.8 – 4.6 kcal/mol (**Table 2**). Notably, GaMD simulations captured dissociation of strychnine from the AC nAChR (**Figures 3** and **S3-S4**) as well as multiple binding events of α-conotoxin RgIA to the AC nAChR (**Figures 4** and **S5-S6**). Overall, the dissociation pathway observed for strychnine in the AC nAChR was the reverse of the first binding pathway observed for α-conotoxin RgIA in the AC nAChR.

Dissociation of the small chemical toxin strychnine from the *Aplysia californica* nAChR

Initially, six molecules of strychnine bound to the AC nAChR, with four orthosteric pockets of nAChR accommodating one strychnine molecule each and one orthosteric pocket containing two strychnine molecules (**Figure 2e**). For this study, we will refer to the two strychnine molecules that bound the same nAChR orthosteric pocket as strychnine-1 and strychnine-2, with strychnine-1 being the inner strychnine molecule that bound the orthosteric pocket more tightly and strychnine-2 being the outer strychnine molecule (**Figure 2e**).

The dissociation of strychnine-1 from nAChR orthosteric pocket observed only once in Sim4 was shown in **Figure 3a** and facilitated by strychnine-1 interactions with strychnine-2 (**Figures 3** and **S3-S4**). A 2D free energy profile based on the strychnine distance to orthosteric pocket (**Figure S2a**) and the opening and closing of the toxin trapping loop (**Figure S2b),** was used to characterize strychnine-1 dissociation from the AC nAChR (**Figure 3b).** The transition of the orthosteric pocket from the closed to opened state was captured as the toxin dissociated since the distance between the COM of the AC-nAChR orthosteric pocket and the COM of residues L29 to D44 and N48 to K61 from the neighboring subunit

increased from ~18 – 22 Å to ~24 – 26 Å (**Figures 3b** and **S3**). Meanwhile, we observed no changes in the Cα-atom distance between residues A:Q100 and D:Q100 (**Figure S3**). We selected four low-energy conformational states from the 2D free energy profile to describe strychnine-1 dissociation from the nAChR, namely states "S1" – "S4". In the "S1" low-energy conformational state, the distance between strychnine-1 and nAChR orthosteric pocket was ~6.9 Å, and the pocket opening/closing distance is ~20.2 Å (**Figure 3c**). Strychnine-1 was located inside the nAChR orthosteric pocket, interacting with residues A:Y55, E:Y93, E:S146-E:W147, and residues E:Y188, E:C190-E:C191, and E:Y195 of the Cys loop in the nAChR orthosteric pocket. Meanwhile, strychnine-2 was located upwards nearby, interacting with residues E:K25, E:P28, and E:G151-E:F152. In state "S2", the distance between strychnine-1 and nAChR orthosteric pocket was ~13.2 Å, while the pocket opening/closing distance is ~24.9 Å, indicating the opening of the orthosteric pocket (**Figure 3d**). In this state, strychnine-2 was observed to go back inside the nAChR orthosteric pocket and interact with strychnine-1 to drag strychnine-1 out of the orthosteric pocket (**Figure 3d**), which resulted in the strychnine-1 dissociation observed in the "S3" low-energy conformational state (**Figure 3e**). In the "S3" state, strychnine-1 was observed to be floating in the bulk solvent while interacting with strychnine-2. Finally, the two toxin molecules broke apart in state "S4", where the distance between strychnine-1 and the nAChR orthosteric pocket was ~35.2 Å, and the orthosteric pocket remained opened at an opening/closing distance of ~24.4 Å (**Figure 3f**). Strychnine-1 moved up to the outside of the nAChR extracellular pore in this state. Overall, strychnine-1 was able to dissociate from the nAChR mainly because of its interactions with the flexible strychnine-2, which dragged the toxin molecule outwards. Strychnine-1 then moved and bound to the outside of the nAChR extracellular pore (**Figure 3a**).

Unlike the other five strychnine molecules that bound tightly to the AC nAChR (**Figures S3**), strychnine-2 binding to the AC nAChR was unstable. In particular, the molecule was observed to dissociate from the nAChR orthosteric pocket in all five simulations (**Figure S4a**). The dissociation pathway of strychnine-2 (**Figure S4b**) was observed to be different from that of strychnine-1 (**Figure 3a**). From its initial position in the nAChR orthosteric

pocket, interacting with residues A:T36, A:Q57, A:M116, A:I118, A:D164, and residues E:C190-E:C191 of the Cys loop in the nAChR orthosteric pocket, strychnine-2 fluctuated and gradually diffused outside of the nAChR orthosteric pocket into the bulk solvent (**Figure S4b**). The phenomenon that two ligand molecules binding to the same orthosteric pocket showed different binding and dissociation pathways has been observed in a previous study[28].

Association of the α-conotoxin RgIA to the *Aplysia californica* and α7-nAChR

We captured two different binding pathways in a total of five binding events across all five simulation replicas (**Figure S5**) of the α-conotoxin RgIA to the AC nAChR orthosteric pocket in the simulation system of AC nAChR with free α-conotoxin RgIA (**Figure S1a**). The first binding pathway was mostly the reverse of the dissociation pathway of strychnine-1 from the nAChR (**Figure 3a**) and described in **Figure 4**. The second binding pathway was a direct binding of the α-conotoxin RgIA from the bulk solvent into the nAChR orthosteric pocket (**Figure S6**), which was the reverse of the dissociation pathway of strychnine-2 from the nAChR (**Figure S4b**).

The nAChR orthosteric pocket was flexible and existed in both opened and closed states in the absence of a bound orthosteric ligand (**Figure S5**). In particular, among five binding events of the α-conotoxin RgIA to the AC-nAChR, the toxin bound to three opened orthosteric pockets in Sim1, Sim2, and Sim3 (**Figure S5**). The orthosteric pocket then became closed in Sim3, with the distance between the COM of the AC-nAChR orthosteric pocket and the COM of residues L29 to D44 and N48 to K61 from the neighboring subunit reduced from ~24 – 27 Å to ~18 – 21 Å, while remained opened in the other two simulations (Sim1 and Sim2) (**Figure S5**). A 2D free energy profile was calculated from the COM distances between Cα atoms of the α-conotoxin RgIA and the AC nAChR orthosteric pockets (**Figure S2a**) and Cα-atom distances between nAChR residues A:Q100 and D:Q100 (**Figure S2c**) in the events that RgIA bind to the AC nAChR (**Figure S5**) to characterize the first binding pathway of α-conotoxin RgIA to the nAChR orthosteric pocket (**Figure 4b**). The Cα-atom distances between nAChR residues A:Q100 and D:Q100 showed no change upon toxin

binding in the AC-nAChR (**Figure S5**). Two low-energy conformational states, namely "S1"-"S2", were selected to describe this first pathway. In the "S1" state, the distance between RgIA and nAChR orthosteric pocket was ~9.1 Å. The α-conotoxin bound to the nAChR orthosteric pocket in this state, interacting with residues B:D77, B:R79, C:S150, C:F152-C:E153, and residues C:Y188-C:E193 and C:Y195 of the Cys loop in the nAChR orthosteric pocket (**Figure 4c**). In the "S2" low-energy conformational state, the distance between RgIA and nAChR orthosteric pocket was ~19.8 Å. In this state, the α-conotoxin of interest was located at the interface between two subunits near the extracellular pore directly above the orthosteric pocket of AC nAChR, interacting with nAChR residues B:D(-2), B:N70-B:E71, B:G73-B:N74, and C:K25-C:D26 (**Figure 4d**). Overall, the first binding pathway of α-conotoxin RgIA to the nAChR involved its movement from the outside of the nAChR extracellular pore to the nAChR orthosteric pocket (**Figure 4a**), which was the reverse of the strychnine-1 dissociation pathway (**Figure 3a**). Meanwhile, in the second binding pathway observed in Sim1, the α-conotoxin RgIA diffused from the bulk solvent directly into the nAChR orthosteric pocket (**Figure S6**), the reverse of the dissociation pathway of strychnine-2 (**Figure S4b**). In an effort to quantify the binding poses of RgIA in the AC-nAChR captured from the GaMD simulations, we calculated the time courses of the number of contacts between the toxins and the nAChR orthosteric pocket in the five binding events (**Figure S7a**) and compared the conformations with the highest number of contacts between the toxin and the receptor to the 7EGR[53] PDB structure (**Figure S7b**). In the 7EGR[53] PDB structure, the five RgIA conotoxins showed from ~28 to ~44 contacts to the nAChR orthosteric pocket. Here, we used a contact definition of ≤ 9Å between Cα atoms. The bound poses with the highest number of contacts obtained from the five binding events were highly similar to the bound pose in the 7EGR[53] PDB structure, with root-mean-square deviation (RMSD) values between ~0.7 and ~1.1 Å (**Figure S7b**). It should be noted that the interactions between α-conotoxins and nAChRs have been studied for the last several decades, and our findings are consistent[4,23,24,54-75].

In the GaMD production simulations of human α7 with free α-conotoxin RgIA (**Figure S1b**), we observed a number of incomplete binding events of the toxin to the receptor that

only involved extracellular ligand binding domains and not the transmembrane helical regions or the intracellular domains (**Figure S8**). In particular, we observed the α-conotoxin approaching the outside of the nAChR orthosteric pocket by diffusing from the outside of the extracellular pore along the nAChR in the GaMD equilibration and Sim1 (**Figure S8a** and **S8b**). The toxin was observed to dissociate directly into the bulk solvent in Sim5 from its unstable binding pose obtained from the GaMD equilibration (**Figure S8c**). We could not capture the entry of the α-conotoxin RgIA into the orthosteric pocket of the α7-nAChR as the toxin was selective towards the α9α10[66] rather than α7 nAChR, demonstrating the consistency between our computational simulations and experimental results.

Effects of toxin binding to nAChRs

For other simulation systems of the nAChR, including the AC nAChR bound by α-conotoxin BuIA (**Figure 2b**), α-conotoxin ImI (**Figure 2c**), α-conotoxin RgIA (**Figure 2d**), pinnatoxin A (**Figure 2f**), and pinnatoxin G (**Figure 2g**), as well as the human α7 nAChR bound by α-bungarotoxin (**Figure 2i**), all the toxins stay bound to the nAChR throughout the simulations (**Figure S9**). To determine the effects of toxin binding to the nAChR, we calculated the average RMSF of the nAChR from the five simulations performed for each nAChR simulation systems. Then, we subtract the nAChR RMSF of the apo receptor from the nAChR RMSF of the systems with toxins bound to determine the changes in receptor flexibility in terms of ΔRMSF upon toxin binding (**Figures S10-S11**). Overall, the AC nAChR became much more rigid, especially at the orthosteric pockets, the extracellular pore, the subunit interfaces, and the interface between the ligand binding domain and transmembrane helix (**Figure S10**), which were the receptor regions that were identified to bind toxins in this and previous study[76]. In addition to these regions, the α-bungarotoxin also made the transmembrane helical domains and horizontal helices at the intracellular domains (i.e., the M4-M4 and M4-MA junctions)[77] of the human α7 nAChR much more rigid (**Figure S11**). Therefore, toxin binding appeared to rigidize all the important regions involved in the gating mechanisms of nAChRs. Since nAChRs belong to the ligand-gated ion channel family[76], we hypothesize that the rigidity caused by the toxins will restrict the necessary movements required by the

nAChRs to open their pores for the ions to pass through, leading to toxicity. The finding was consistent with the closing gating mechanism observed in the resting states of antagonist-bound nAChRs[5].

To confirm our hypothesis that the binding to toxin modulates the gating mechanism, we performed principal component analysis (PCA) to determine the primary motions of the nAChR simulation systems in the presence and absence of the toxins (**Figure S12**). In the apo AC nAChR, the primary motions involved major outwards movements of the outside of the extracellular pore, the outward movements of the loop regions and the subunit interfaces in the nAChR orthosteric pockets, and the inward movements of the loop regions towards the subunit interfaces in the nAChR orthosteric pockets (**Figure S12a**). Similar primary motions were observed in the apo human α7 nAChR, and we also observed minor movements at the horizontal helices located at the interface of the transmembrane helical and intracellular domains (**Figure S12h**). Upon binding of the toxins to the nAChRs, the nAChR orthosteric pockets were rigidized, and no primary motion was observed at the nAChR orthosteric pockets (**Figure S12b-S12g** and **S12i**). However, we observed major closing motions at the outside of the extracellular pores of the soluble ligand binding domains and the horizontal helices at the interface of the transmembrane helical and intracellular domains, the two regions known to serve as the gates for the entrance of ions through the nAChRs[77]. In particular, we observed two opposite subunits moving towards another to close the extracellular pores in the AC nAChRs bound by α-conotoxin BuIA (**Figure S12b**), strychnine (**Figure S12e**), and pinnatoxin A (**Figure S12f**). The horizontal helices at the interface of the transmembrane helical and intracellular domains (i.e., the M4-M4 and M4-MA junctions)[77] were observed to move strongly towards their neighbors in the presence of the α-bungarotoxin in the human α7 nAChR (**Figure S12i**). Therefore, through the closing gating mechanism, the toxins enacted their toxicity in the nAChRs by preventing the ions from diffusing through the channels[77].

Discussion

While it is known that various ligands, including toxins of different physical and structural properties, bind to the same orthosteric pockets in the nAChRs, the reason remains unclear. Furthermore, the binding and dissociation pathways of toxins to the nAChRs and the associated descriptors have been underexplored for several reasons, which hinders the efforts to develop effective antidotes for the toxins. In this work, we have performed extensive all-atom dual-boost GaMD simulations on several nAChR systems with toxins, including α-conotoxins BuIA, ImI, and RgIA, strychnine, pinnatoxin A, pinnatoxin G, and α-bungarotoxin for a total of 60 μs of simulation time to determine the descriptors associated with binding of toxins in the nAChRs.

We captured two common binding and dissociation pathways that were shared across the toxins (α-conotoxin RgIA and strychnine). In the first binding pathway of toxins to the nAChR, the toxins gradually diffused from the bulk solvent to first bind near the extracellular pore of the ligand binding domain of the nAChR, then moved downwards along the nAChR to the orthosteric pockets (**Figures 4a** and **S8a-b**). In the second binding pathway, the toxins diffused directly from the bulk solvents into the nAChR orthosteric pockets (**Figure S6**). The dissociation pathways of the toxins from the nAChR were the direct reverse of the observed binding pathways (**Figures 3a, S4b,** and **S8c**). The second binding and dissociation pathways we observed for toxins in the nAChRs were highly similar to the binding pathway of the γ-aminobutyric acid (GABA) neurotransmitter to the GABA type A receptors identified from a previous study[78]. In an effort to determine which binding pathway is more dominant, we carried out GaMD simulations of the binding of the endogenous ligand acetylcholine to the AC nAChR (**Figure S13a**). Due to its small nature, GaMD simulations were able to rapidly capture complete binding of most to all acetylcholine molecules in the five available nAChR orthosteric pockets at the same time starting from their unbound states (**Figure S13b-S13f**). We observed that the acetylcholine molecule mostly diffused directly from the bulk solvent into the nAChR orthosteric pocket (**Figure S14a, S14b, S14c,** and **S14e**), even though it sometimes first bound to the outside of the extracellular pore before diffusing along the receptor down to the nAChR orthosteric pocket (**Figure S14d**). Therefore, the second binding pathway, or the "direct diffusion" pathway, appeared to be preferred pathway for small

molecules/ligands. However, for peptides like α-conotoxins, the ligands might prefer to first "dock" to the receptor at the outside of the extracellular pore first before diffusing downwards and wait for the nAChR orthosteric pocket to open to enter the pocket, as observed in the GaMD simulations of the α-conotoxin RgIA binding to the AC and α7-nAChR (**Figures 4a** and **S8**). We hypothesized that different toxins/ligands of different sizes may prefer different binding pathways. Nevertheless, ligand binding to the nAChR orthosteric pocket could be overall considered "diffusion" binding, regardless of the pathways taken, due to the exposed nature of the pocket.

In an effort to explain the common binding and dissociation pathways observed across different toxins and nAChRs, we plotted the electrostatic potentials[79] for the nAChRs and protein toxins (α-conotoxins BuIA, ImI, and RgIA and α-bungarotoxin) (**Figure 5** and **S15**). First, we observed that the orthosteric pockets of nAChR were electrostatically bipolar: the inner side of the loop that connected the two β-strands was negative potential, while its opposite side to the right (located at the interface of the subunits) was mostly positive potential (**Figure 5a**). Therefore, this binding pocket was highly suitable to accommodate toxins such as α-conotoxins BuIA, ImI, and RgIA and α-bungarotoxin, with their regions of contacts to the binding pocket also being bipolar (**Figure 5b-5d,** and **S15**). The positive potential side of the toxins could stably interact with the inner side of the nAChR loop, while the negative potential side could face the positive potential side of the nAChR orthosteric pocket (**Figure 5**). This phenomenon was also observed for the endogenous ligand of the nAChR, acetylcholine (**Figure S16**). In particular, the native ligand, acetylcholine, also had a positively charged tail ($-N(CH_3)_3^+$) and a negative potential end ($-O-C(=O)-CH_3$). The orientation of acetylcholine was the same as the toxins, with the positively charged end favorably interacting with the negative potential nAChR loop while the negative potential end interacted with the opposite side (**Figure S16**). We also calculated the dipole moments (μ) for the toxins examined in this study and acetylcholine (**Table 4**). The smallest dipole was found for pinnatoxin G at ~3.0 D, the highest dipole was found for α-bungarotoxin at ~328.7 D (**Table 4**). These results demonstrated the importance of electrostatic potential complementarity in the selective binding of toxins in the nAChR. Notably, this determinant

has been proposed as important for toxin/ligand binding in the nAChR and other neuronal receptors[56,78,80].

In conclusion, we have captured general binding pathways of the toxins to the nAChRs in our GaMD simulations and found that the electrostatic potentials played an important role in explaining the common binding pockets and binding pathways of toxins to the nAChRs. Based on our findings, we predict that drugs that are designed with proper shapes and to be highly electrostatically bipolar could serve as potential antidotes for α-conotoxins and many other toxins in general as they could bind tightly to the toxins. We intend to extend the current study, which provided important mechanistic insights into the binding of diverse toxins to the nAChRs, to include much more toxins and different subunits of the nAChRs. Given the limited availability of experimental toxin-bound nAChR structures, these models are expected to augment structure and binding prediction tools such as AlphaFold2[81] and RosetTTAFold[82]. Furthermore, we will apply selective GaMD methods, including ligand/peptide GaMD[83-86], to explore the kinetics of various toxin binding to the nAChRs, including their residence times, association and dissociation rate constants.

Declaration of Interest

The authors declare no conflicts of interest.

Acknowledgements

This work was supported by the Defense Threat Reduction Agency (award no. HDTRA1345035). We would like to thank Elizabeth Clarke, Daniel Jacobsen, Hannah Whitacre, Yinglong Miao, and Jinan Wang for insightful discussions. This work was performed at the Los Alamos National Laboratory (LANL), operated by Triad National Security, LLC, for the National Nuclear Security Administration of the U.S. Department of Energy (contract 89233218CNA000001). Computational resources were provided by LANL Institutional Computing. The authors would like to thank Daphne Stanley for supporting this work.

Author Contributions

H.N.D. performed research, analyzed data, and wrote the manuscript. J.Z.K. acquired funding, supervised the research, and wrote the manuscript. S.G. supervised the research, analyzed data, and wrote the manuscript. All authors contributed to the final version of the manuscript.

References

1. Ho, T.N.T., Abraham, N., and Lewis, R.J. (2020). Structure-Function of Neuronal Nicotinic Acetylcholine Receptor Inhibitors Derived from Natural Toxins. Frontiers in Neuroscience *14*, 609005. https://doi.org/10.3389/fnins.2020.609005.
2. Hogg, R.C., Raggenbass, M., and Bertand, D. (2003). Nicotinic acetylcholine receptors: from structure to brain function (Springer). 10.1007/s10254-003-0005-1.
3. Albuquerque, E.X., Pereira, E.F.R., Alkondon, M., and Rogers, S.W. (2009). Mammalian nicotinic acetylcholine receptors: from structure to function. Physiological Reviews *89*, 73-120. https://doi.org/10.1152/physrev.00015.2008.
4. Dutertre, S., Nicke, A., Tyndall, J.D.A., and Lewis, R.J. (2004). Determination of alpha-conotoxin binding modes on neuronal nicotinic acetylcholine receptors. Journal of Molecular Recognition *17*, 339-347. https://doi.org/10.1002/jmr.683.
5. Noviello, C.M., Gharpure, A., Mukhtasimova, N., Cabuco, R., Baxter, L., Borek, D., Sine, S.M., and Hibbs, R.E. (2021). Structure and gating mechanism of the α7 nicotinic acetylcholine receptor. Cell *184*, 2121-2134.e2113. https://doi.org/10.1016/j.cell.2021.02.049.
6. Bekbossynova, A., Zharylgap, A., and Filchakova, O.M. (2021). Venom-Derived Neurotoxins Targeting Nicotinic Acetylcholine Receptors. Molecules *26*, 3373. https://doi.org/10.3390/molecules26113373.
7. Prashanth, J.R., Brust, A., Jin, A.H., Alewood, P.F., Dutertre, S., and Lewis, R.J. (2014). Cone snail venomics: From novel biology to novel therapeutics. Future Medicinal Chemistry *6*, 1659-1675. 10.4155/fmc.14.99.
8. Vetter, I., and Lewis, R.J. (2012). Therapeutic potential of cone snail venom peptides (conopeptides). Curr. Top. Med. Chem. *12*, 1546–1552. 10.2174/156802612802652457.
9. Gao, B., Peng, C., Yang, J., Yi, Y., Zhang, J., and Shi, Q. (2017). Cone Snails: A Big Store of Conotoxins for Novel Drug Discovery. Toxins *9*, 397. 10.3390/toxins9120397.
10. Tae, H.-S., and Adams, D.J. (2023). Nicotinic acetylcholine receptor subtype expression, function, and pharmacology: Therapeutic potential of α-conotoxins. Pharmacological Research *191*, 106747. https://doi.org/10.1016/j.phrs.2023.106747.
11. Davis, J., Jones, A., and Lewis, R.J. (2009). Remarkable inter- and intra-species complexity of conotoxins revealed by LC/MS. Peptides *30*, 1222-1227. https://doi.org/10.1016/j.peptides.2009.03.019.

12. Kaas, Q., Westermann, J.-C., and Craik, D.J. (2010). Conopeptide characterization and classifications: An analysis using ConoServer. Toxicon *55*, 1491-1509. https://doi.org/10.1016/j.toxicon.2010.03.002.
13. Young, H.S., Herbette, L.G., and Skita, V. (2003). α-Bungarotoxin Binding to Acetylcholine Receptor Membranes Studied by Low Angle X-Ray Diffraction. Biophysical Journal *85*, 943-953. https://doi.org/10.1016/S0006-3495(03)74533-0.
14. Balass, M., Katchalski-Katzir, E., and Fuchs, S. (1997). The α-bungarotoxin binding site on the nicotinic acetylcholine receptor: Analysis using a phage–epitope library. PNAS *94*, 6054-6058. https://doi.org/10.1073/pnas.94.12.6054.
15. Garcia-Colunga, J., and Miledi, R. (1999). Modulation of nicotinic acetylcholine receptors by strychnine. PNAS *96*, 4113-4118. https://doi.org/10.1073/pnas.96.7.4113.
16. Brams, M., Pandya, A., Kuzmin, D., Van Elk, R., Krijnen, L., Yakel, J.L., Tsetlin, V., Smit, A.B., and Ulens, C. (2011). A Structural and Mutagenic Blueprint for Molecular Recognition of Strychnine and D-Tubocurarine by Different Cys-Loop Receptors. PLoS Biology *9*, 01034. https://doi.org/10.1371/journal.pbio.1001034.
17. Bourne, Y., Sulzenbacher, G., Radic, Z., Araoz, R., Reynaud, M., Benoit, E., Zakarian, A., Servent, D., Molgo, J., Taylor, P., and Marchot, P. (2015). Marine Macrocyclic Imines, Pinnatoxins A and G: Structural Determinants and Functional Properties to Distinguish Neuronal alpha 7 from Muscle alpha 12 beta gamma delta nAChRs. Structure *23*, 1106-1115. https://doi.org/10.1016/j.str.2015.04.009.
18. Karplus, M., and McCammon, J.A. (2002). Molecular dynamics simulations of biomolecules. Nature Structural and Molecular Biology *9*, 646-652.
19. Mansbach, R.A., Travers, T., McMahon, B.H., Fair, J.M., and Gnanakaran, S. (2019). Snails In Silico: A Review of Computational Studies on the Conopeptides. Marine Drugs *17*, 145.
20. Beissner, M., Dutertre, S., Schemm, R., Danker, T., Sporning, A., Grubmuller, H., and Nicke, A. (2012). Efficient Binding of 4/7 α-Conotoxins to Nicotinic α4β2 Receptors Is Prevented by Arg185 and Pro195 in the α4 Subunit. Molecular Pharmacology *82*, 711-718. 10.1124/mol.112.078683.
21. Yu, R., Craik, D.J., and Kaas, Q. (2011). Blockade of Neuronal α7-nAChR by α-Conotoxin ImI Explained by Computational Scanning and Energy Calculations. PLOS Computational Biology *7*, e1002011. 10.1371/journal.pcbi.1002011.
22. Cuny, H., Kompella, S.N., Tae, H.S., Yu, R., and Adams, D.J. (2016). Key Structural Determinants in the Agonist Binding Loops of Human β2 and β4 Nicotinic Acetylcholine Receptor Subunits Contribute to α3β4 Subtype Selectivity of α-Conotoxins. Journal of Biological Chemistry *291*, 23779–23792. 10.1074/jbc.M116.730804.
23. Pucci, L., Grazioso, G., Dallanoce, C., Rizzi, L., De Micheli, C., Clementi, F., Bertrand, S., Bertrand, D., Longhi, R., De Amici, M., and Gotti, C. (2011). Engineering of α-conotoxin MII-derived peptides with increased selectivity for native α6β2* nicotinic acetylcholine receptors. FASEB Journal *25*, 3775-3789. 10.1096/fj.10-179853

24. Yu, R., Kompella, S.N., Adams, D.J., Craik, D.J., and Kaas, Q. (2013). Determination of the α-Conotoxin Vc1.1 Binding Site on the α9α10 Nicotinic Acetylcholine Receptor. Journal of Medicinal Chemistry *56*, 3557-3567. 10.1021/jm400041h.
25. Suresh, A., and Hung, A. (2016). Molecular Simulation study of the unbinding of α-conotoxin [Y4E]GID at the α7 and α4β2 neuronal nicotinic acetylcholine receptors. Journal of Molecular Graphics and Modelling *70*, 109-121. 10.1016/j.jmgm.2016.09.006.
26. Yu, R., Kaas, Q., and Craik, D.J. (2012). Delineation of the Unbinding Pathway of α-Conotoxin ImI from the α7 Nicotinic Acetylcholine Receptor. The Journal of Physcial Chemistry B *116*, 6097-6105. 10.1021/jp301352d.
27. Miao, Y., Feher, V.A., and McCammon, J.A. (2015). Gaussian accelerated molecular dynamics: unconstrained enhanced sampling and free energy calculation. Journal of Chemical Theory and Computation *11*, 3584-3595.
28. Do, H.N., Akhter, S., and Miao, Y. (2021). Pathways and Mechanism of Caffeine Binding to Human Adenosine A2A Receptor. Frontiers in Molecular Biosciences *8*, 242.
29. Do, H.N., Wang, J., and Miao, Y. (2023). Deep Learning Dynamic Allostery of G-Protein-Coupled Receptors. JACS Au *3*, 3165-3180. https://pubs.acs.org/doi/10.1021/jacsau.3c00503.
30. Waterhouse, A., Bertoni, M., Bienert, S., Studer, G., Tauriello, G., Gumienny, R., Heer, F., de Beer, T., Rempfer, C., Bordoli, L., et al. (2018). SWISS-MODEL: homology modelling of protein structures and complexes. Nucleic Acids Research *46*, W296-W303.
31. Jo, S., Kim, T., Iyer, V., and Im, W. (2008). CHARMM-GUI: A Web-based Graphical User Interface for CHARMM. Journal of Computational Chemistry *29*, 1859-1865.
32. Wu, E., Cheng, X., Jo, S., Rui, H., Song, K., Davila-Contreras, E., Qi, Y., Lee, J., Monje-Galvan, V., Venable, R., et al. (2014). CHARMM-GUI Membrane Builder Toward Realistic Biological Membrane Simulations. Journal of Computational Chemistry *35*, 1997-2004.
33. Lee, J., Hitzenberger, M., M. Rieger, N.R. Kern, M. Zacharias, and Im, W. (2020). CHARMM-GUI supports the Amber force fields. Journal of Chemical Physics *153*, 035103.
34. Filchakova, O.M., Talley, T.T., Reger, A.S., Kim, C., Ho, K., Han, K., Taylor, P., and McIntosh, J.M. (2012). Pairwise interaction of alpha-conotoxin BuIA Pro6 with the beta subunit of nicotinic acetylcholine receptor. To be published.
35. Ponder, J.W., and Case, D.A. (2003). Force fields for protein simulations. Advances in Protein Chemistry *66*, 27-85.
36. Maier, J.A., Martinez, C., Kasavajhala, K., Wickstrom, L., Hauser, K.E., and Simmerling, C. (2015). ff14SB: Improving the Accuracy of Protein Side Chain and Backbone Parameters from ff99SB. Journal of Chemical Theory and Computation *11*, 3696-3713. https://doi.org/10.1021/acs.jctc.5b00255.
37. Wang, J., Wolf, R., Caldwell, J., Kollman, P., and Case, D. (2004). Development and testing of a general AMBER force field. Journal of Computational Chemistry *25*, 1157-1174.

38. Jakalian, A., Jack, D.B., and Bayly, C.I. (2002). Fast, efficient generation of high-quality atomic charges. AM1-BCC model: II. Parameterization and validation. Journal of Computational Chemistry *23*, 1623-1641.
39. Jorgensen, W., Chandrasekhar, J., Madura, J., Impey, R., and Klein, M. (1983). Comparison of simple potential functions for simulating liquid water. Journal of Chemical Physics *79*, 926-935.
40. Case, D.A., Aktulga, H.M., Belfon, K., Ben-Shalom, I.Y., Berryman, J.T., Brozell, S.R., Cerutti, D.S., Cheatham, I., T.E. , Cisneros, G.A., Cruzeiro, V.W.D., et al. (2023). Amber 2023. University of California, San Francisco.
41. Ryckaert, J.-P., Ciccotti, G., and Berendsen, H.J.C. (1977). Numerical integration of the cartesian equations of motion of a system with constraints: molecular dynamics of n-alkanes. Journal of Computational Physics *23*, 327-341.
42. Evans, D.J. (1983). Computer "experiment" for nonlinear thermodynamics of Couette flow. The Journal of Chemical Physics *78*, 3297.
43. Hoover, W.G., Ladd, A.J.C., and Moran, B. (1982). High-Strain-Rate Plastic Flow Studied via Nonequilibrium Molecular Dynamics. Physical Review Letters *48*, 1818.
44. Essmann, U., Perera, L., Berkowitz, M.L., Darden, T., Lee, H., and Pedersen, L.G. (1995). A Smooth Particle Mesh Ewald Method. Journal of Chemical Physics *103*.
45. Berendsen, H.J.C., Postma, J.P.M., Vangunsteren, W.F., Dinola, A., and Haak, J.R. (1984). Molecular Dynamics with Coupling to an External Bath. Journal of Chemical Physics *81*, 3684-3690.
46. Wang, J., Arantes, P., Bhattarai, A., Hsu, R.V., Pawnikar, S., Huang, Y.-M., Palermo, G., and Miao, Y. (2021). Gaussian accelerated molecular dynamics: Principles and applications. WIREs Computational Molecular Science *11*, e1521. https://doi.org/10.1002/wcms.1521.
47. Roe, D.R., and Cheatham, I.T.E. (2013). PTRAJ and CPPTRAJ: software for processing and analysis of molecular dynamics trajectory data. Journal of Chemical Theory and Computation *9*, 3084-3095.
48. Case, D.A., Aktulga, H.M., Belfon, K., Cerutti, D.S., Cisneros, G.A., Cruzeiro, V.W.D., Forouzesh, N., Giese, T.J., Götz, A.W., Gohlke, H., et al. (2023). AmberTools. Journal of Chemical Information and Modeling *63*, 6183-6191. https://doi.org/10.1021/acs.jcim.3c01153.
49. Miao, Y., Sinko, W., Pierce, L., Bucher, D., Walker, R.C., and McCammon, J.A. (2014). Improved reweighting of accelerated molecular dynamics simulations for free energy calculation. Journal of Chemical Theory and Computation *10*, 2677-2689.
50. Hansen, S.B., Sulzenbacher, G., Huxford, T., Marchot, P., Taylor, P., and Bourne, Y. (2005). Structures of Aplysia Achbp Complexes with Nicotinic Agonists and Antagonists Reveal Distinctive Binding Interfaces and Conformations. EMBO Journal *24*, 3635-3646. https://doi.org/10.1038/sj.emboj.7600828.
51. Case, D.A., Belfon, K., Ben-Shalom, I.Y., Brozell, S.R., Cerutti, D.S., Cheatham, T.E., Cruzeiro, V.W.D., Darden, T., Duke, R.E., and Giambasu, G. (2020). AMBER 2020.
52. Humphrey, W., Dalke, A., and Schulten, K. (1996). VMD: visual molecular dynamics. Journal of Molecular Graphics and Modelling *14*, 33-38.

53. Wang, X.Q., Pan, S., Fan, Y.X., Xue, Y., Zhu, X.P., and Luo, S.L. (2021). Co-crystal structure of Ac-AChBPP in complex with RgIA. To be published.
54. Kaas, Q., Yu, R., Jin, A.H., Dutertre, S., and Craik, D.J. (2012). ConoServer: updated content, knowledge, and discovery tools in the conopeptide database. Nucleic Acids Research *40*, D325-330.
55. Olivera, B.M., Quik, M., Vincler, M., and McIntosh, J.M. (2008). Subtype-selective conopeptides targeted to nicotinic receptors: Concerted discovery and biomedical applications. Channels *2*, 143-152. https://doi.org/10.4161/chan.2.2.6276.
56. Akondi, K.B., Muttenthaler, M., Dutertre, S., Kaas, Q., Craik, D.J., Lewis, R.J., and Alewood, P.F. (2014). Discovery, Synthesis, and Structure–Activity Relationships of Conotoxins. Chemical Reviews *114*, 5815-5847. https://doi.org/10.1021/cr400401e.
57. Chu, X., Tae, H.-S., Xu, Q., Jiang, T., Adams, D.J., and Yu, R. (2019). α-Conotoxin Vc1.1 Structure–Activity Relationship at the Human α9α10 Nicotinic Acetylcholine Receptor Investigated by Minimal Side Chain Replacement. ACS Chemical Neuroscience *10*, 4328-4336. https://doi.org/10.1021/acschemneuro.9b00389.
58. Liang, J., Tae, H.-S., Zhao, Z., Li, X., Zhang, J., Chen, S., Jiang, T., Adams, D.J., and Yu, R. (2022). Mechanism of Action and Structure–Activity Relationship of α-Conotoxin Mr1.1 at the Human α9α10 Nicotinic Acetylcholine Receptor. Journal of Medicinal Chemistry *65*, 16204-16217. https://doi.org/10.1021/acs.jmedchem.2c00494.
59. Jin, A.H., Muttenthaler, M., Dutertre, S., Himaya, S.W.A., Kaas, Q., Craik, D.J., Lewis, R.J., and Alewood, P.F. (2019). Conotoxins: Chemistry and Biology. Chemical Reviews *119*, 11510-11549. https://doi.org/10.1021/acs.chemrev.9b00207.
60. Turner, M.W., Marquart, L.A., Phillips, P.D., and McDougal, O.M. (2019). Mutagenesis of α-Conotoxins for Enhancing Activity and Selectivity for Nicotinic Acetylcholine Receptors. Toxins *11*, 113. 10.3390/toxins11020113.
61. Lin, B., Xiang, S., and Li, M. (2016). Residues Responsible for the Selectivity of α-Conotoxins for Ac-AChBP or nAChRs. Marine Drugs *14*, 173. 10.3390/md14100173.
62. Wang, S., Zhao, C., Liu, Z., Wang, X., Liu, N., Du, W., and Dai, Q. (2015). Structural and Functional Characterization of a Novel α-Conotoxin Mr1.7 from Conus marmoreus Targeting Neuronal nAChR α3β2, α9α10 and α6/α3β2β3 Subtypes. Marine Drugs *13*, 3259-3275. 10.3390/md13063259.
63. George, A.A., John, S.J., Lucero, L.M., Eaton, J.B., Jaiswal, E., Christensen, S.B., Gajewiak, J., Watkins, M., Cao, Y., Olivera, B.M., et al. (2024). Analogs of α-conotoxin PnIC selectively inhibit α7β2- over α7-only subtype nicotinic acetylcholine receptors via a novel allosteric mechanism. The FASEB Journal *38*, e23374. 10.1096/fj.202302079.
64. Dowell, C., Olivera, B.M., Garrett, J.E., Staheli, S.T., Watkins, M., Kuryatov, A., Yoshikami, D., Lindstrom, J.M., and McIntosh, J.M. (2003). α-Conotoxin PIA Is Selective for α6 Subunit-Containing Nicotinic Acetylcholine Receptors. The Journal of Neuroscience *23*, 8445-8452. 10.1523/JNEUROSCI.23-24-08445.2003.
65. Lebbe, E.K.M., Peigneur, S., Wijesekara, I., and Tytgat, J. (2014). Conotoxins Targeting Nicotinic Acetylcholine Receptors: An Overview. Marine Drugs *12*, 2970-3004. 10.3390/md12052970.

66. Ellison, M., Haberlandt, C., Gomez-Casati, M.E., Watkins, M., Elgoyhen, A.B., McIntosh, J.M., and Olivera, B.M. (2006). α-RgIA: A Novel Conotoxin That Specifically and Potently Blocks the α9α10 nAChR. Biochemistry *45*, 1511-1517. https://doi.org/10.1021/bi0520129.
67. Luo, S., Nguyen, T.A., Cartier, G.E., Olivera, B.M., Yoshikami, D., and McIntosh, J.M. (1999). Single-Residue Alteration in α-Conotoxin PnIA Switches Its nAChR Subtype Selectivity. Biochemistry *38*, 14542-14548. https://doi.org/10.1021/bi991252j.
68. Hone, A.J., Scadden, M., Gajewiak, J., Christensen, S.B., Lindstrom, J.M., and McIntosh, J.M. (2012). α-Conotoxin PeIA[S9H,V10A,E14N] Potently and Selectively Blocks α6β2β3 versus α6β4 Nicotinic Acetylcholine Receptors. Molecular Pharmacology *82*, 972-982. 10.1124/mol.112.080853.
69. Luo, S., Zhangsun, D., Harvey, P.J., Kaas, Q., Wu, Y., Zhu, X., Hu, Y., Li, X., Tsetlin, V.I., Christensen, S., et al. (2015). Cloning, synthesis, and characterization of αO-conotoxin GeXIVA, a potent α9α10 nicotinic acetylcholine receptor antagonist. PNAS *112*, E4026-E4035. https://doi.org/10.1073/pnas.1503617112.
70. Peng, C., Han, Y., Sanders, T., Chew, G., Liu, J., Hawrot, E., Chi, C., and Wang, C. (2008). alpha4/7-conotoxin Lp1.1 is a novel antagonist of neuronal nicotinic acetylcholine receptors. Peptides *29*, 1700-1707. 10.1016/j.peptides.2008.05.028.
71. Luo, S., Zhangsun, D., Schroeder, C.I., Zhu, X.P., Hu, Y., Wu, Y., Weltzin, M.M., Eberhard, S., Kaas, Q., Craik, D.J., et al. (2014). A novel α4/7-conotoxin LvIA from Conus lividus that selectively blocks α3β2 vs. α6/α3β2β3 nicotinic acetylcholine receptors. The FASEB Journal *28*, 1842-1853. 10.1096/fj.13-244103.
72. Guo, M., Yu, J., Zhu, X., Zhangsun, D., and Luo, S. (2021). Characterization of an α 4/7-Conotoxin LvIF from Conus lividus That Selectively Blocks α3β2 Nicotinic Acetylcholine Receptor. Marine Drugs *19*, 398. 10.3390/md19070398.
73. Armishaw, C.J. (2010). Synthetic α-Conotoxin Mutants as Probes for Studying Nicotinic Acetylcholine Receptors and in the Development of Novel Drug Leads. Toxins *2*, 1471-1499. 10.3390/toxins2061471.
74. Xu, P., Kaas, Q., Wu, Y., Zhu, X., Li, X., Harvey, P.J., Zhangsun, D., Craik, D.J., and Luo, S. (2020). Structure and Activity Studies of Disulfide-Deficient Analogues of αO-Conotoxin GeXIVA. Journal of Medicinal Chemistry *63*, 1564-1575. https://doi.org/10.1021/acs.jmedchem.9b01409.
75. Ulens, C., Hogg, R.C., Celie, P.H., Bertrand, D., Tsetlin, V., Smit, A.B., and Sixma, T.K. (2006). Structural determinants of selective α-conotoxin binding to a nicotinic acetylcholine receptor homolog AChBP. PNAS *103*, 3615-3620. https://doi.org/10.1073/pnas.0507889103.
76. Iturriaga-Vasquez, P., Alzate-Morales, J., Bermudez, I., Varas, R., and Reyes-Parada, M. (2015). Multiple binding sites in the nicotinic acetylcholine receptors: An opportunity for polypharmacolgy. Pharmacological Research *101*, 9-17.
77. Noviello, C.M., Gharpure, A., Mukhtasimova, N., Cabuco, R., Baxter, L., Borek, D., Sine, S.M., and Hibbs, R.E. (2021). Structure and gating mechanism of the alpha7 nicotinic acetylcholine receptor. Cell *184*, 2121-2134.e2113. https://doi.org/10.1016/j.cell.2021.02.049.

78. Carpenter, T.S., and Lightstone, F.C. (2016). An Electrostatic Funnel in the GABA-Binding Pathway. PLOS Computational Biology *12*, e1004831. 10.1371/journal.pcbi.1004831.
79. Schrodinger, L., and DeLano, W. (2020). The PyMOL Molecular Graphics System, Version 2.5.0. Schrodinger, LLC.
80. Haufe, Y., Kuruva, V., Samanani, Z., Lokaj, G., Kamnesky, G., Shadamarshan, P.K., Shahoei, R., Katz, D., Sampson, J.M., Pusch, M., et al. (2023). Basic Residues at Position 11 of α-Conotoxin LvIA Influence Subtype Selectivity between α3β2 and α3β4 Nicotinic Receptors via an Electrostatic Mechanism. ACS Chemical Neuroscience *14*, 4311-4322. https://doi.org/10.1021/acschemneuro.3c00506.
81. Jumper, J., Evans, R., Pritzel, A., Green, T., Figurnov, M., Ronneberger, O., Tunyasuvunakool, K., Bates, R., Zidek, A., Potapenko, A., et al. (2021). Highly accurate protein structure prediction with AlphaFold. Nature *596*, 583-589. https://doi.org/10.1038/s41586-021-03819-2.
82. Baek, M., DiMaio, F., Anischenko, I., Dauparas, J., Ovchinnikov, V., Lee, G.R., Wang, J., Cong, Q., Kinch, L.N., Schaeffer, R.D., et al. (2021). Accurate prediction of protein structures and interactions using a three-track neural network. Science *373*, 871-876.
83. Miao, Y., Bhattarai, A., and Wang, J. (2020). Ligand Gaussian accelerated molecular dynamics (LiGaMD): characterization of ligand binding thermodynamics and kinetics. Journal of Chemical Theory and Computation *16*, 5526-5547.
84. Wang, J., and Miao, Y. (2023). Ligand Gaussian Accelerated Molecular Dynamics 2 (LiGaMD2): Improved Calculations of Ligand Binding Thermodynamics and Kinetics with Closed Protein Pocket. Journal of Chemical Theory and Computation *19*, 733-745.
85. Wang, J., and Miao, Y. (2024). Ligand Gaussian Accelerated Molecular Dynamics 3 (LiGaMD3): Improved Calculations of Binding Thermodynamics and Kinetics of Both Small Molecules and Flexible Peptides. Journal of Chemical Theory and Computation *20*, 5829-5841. https://doi.org/10.1021/acs.jctc.4c00502.
86. Wang, J., and Miao, Y. (2020). Peptide Gaussian accelerated molecular dynamics (Pep-GaMD): enhanced sampling and free energy and kinetics calculations of peptide binding. Journal of Chemical Physics *153*, 154109.
87. Rogers, J.P., Luginbuhl, P., Pemberton, K., Harty, P., Wemmer, D.E., and Stevens, R.C. (2000). Structure-Activity Relationships in a Peptidic α7 Nicotinic Acetylchone Receptor Antagonist. Journal of Molecular Biology *304*, 911-926. https://doi.org/10.1006/jmbi.2000.4247.
88. Vincent, A., Jacobson, L., and Curran, L. (1998). α-Bungarotoxin binding to human muscle acetylcholine receptor measurement of affinity delineation of AChR subunit residues crucial to binding and protection of AChR function by synthetic peptides. Neurochemistry International *32*, 427-433. 10.1016/s0197-0186(97)00118-6.
89. Hansen, S.B., Talley, T.T., Radic, Z., and Taylor, P. (2004). Structural and ligand recognition characteristics of an acetylcholine-binding protein from Aplysia californica. Journal of Biological Chemistry *279*, 24197-24202. 10.1074/jbc.M402452200.

90. Zhao, Y., Liu, S., Zhou, Y., Zhang, M., Chen, H., Eric Xu, H., Sun, D., Liu, L., and Tian, C. (2021). Structural basis of human alpha 7 nicotinic acetylcholine receptor activation. Cell Research *31*, 713-716. https://doi.org/10.1038/s41422-021-00509-6.

Figures

Figure 1. Structures of toxins explored in this study, including **(a)** α-conotoxin BulA, **(b)** α-conotoxin Iml, **(c)** α-conotoxin RglA, **(d)** strychnine, **(e)** pinnatoxin A, **(f)** pinnatoxin G, and **(g)** α-bungarotoxin. The heteroatoms shown as sticks are colored as following: nitrogen (blue), oxygen (red), hydrogen (white), and sulfur (dark yellow). The PDB IDs of the structures are included in **Table 2**.

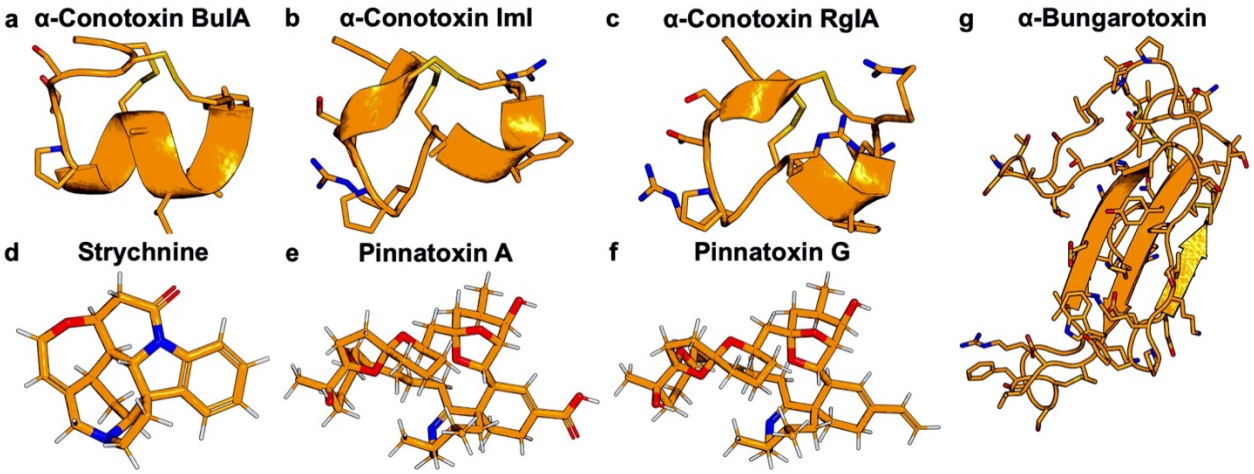

Figure 2. Simulation systems of nicotinic acetylcholine receptors (nAChRs) bound by toxins. (a) Apo Aplysia californica (AC) nAChR. **(b)** AC nAChR bound by α-conotoxin BulA. **(c)** AC nAChR bound by α-conotoxin Iml. **(d)** AC nAChR bound by α-conotoxin RglA. **(e)** AC nAChR bound by strychnine. **(f)** AC nAChR bound by pinnatoxin A. **(g)** AC nAChR bound by pinnatoxin G. **(h)** Apo human α7 nAChR. **(i)** Human α7 nAChR bound by α-bungarotoxin. The nAChRs are colored green, while the toxins are colored orange. The POPC membrane lipid bilayers were shown in **(h-i)**. Additional simulation systems of toxin binding to the nAChRs were included in **Figure S1**.

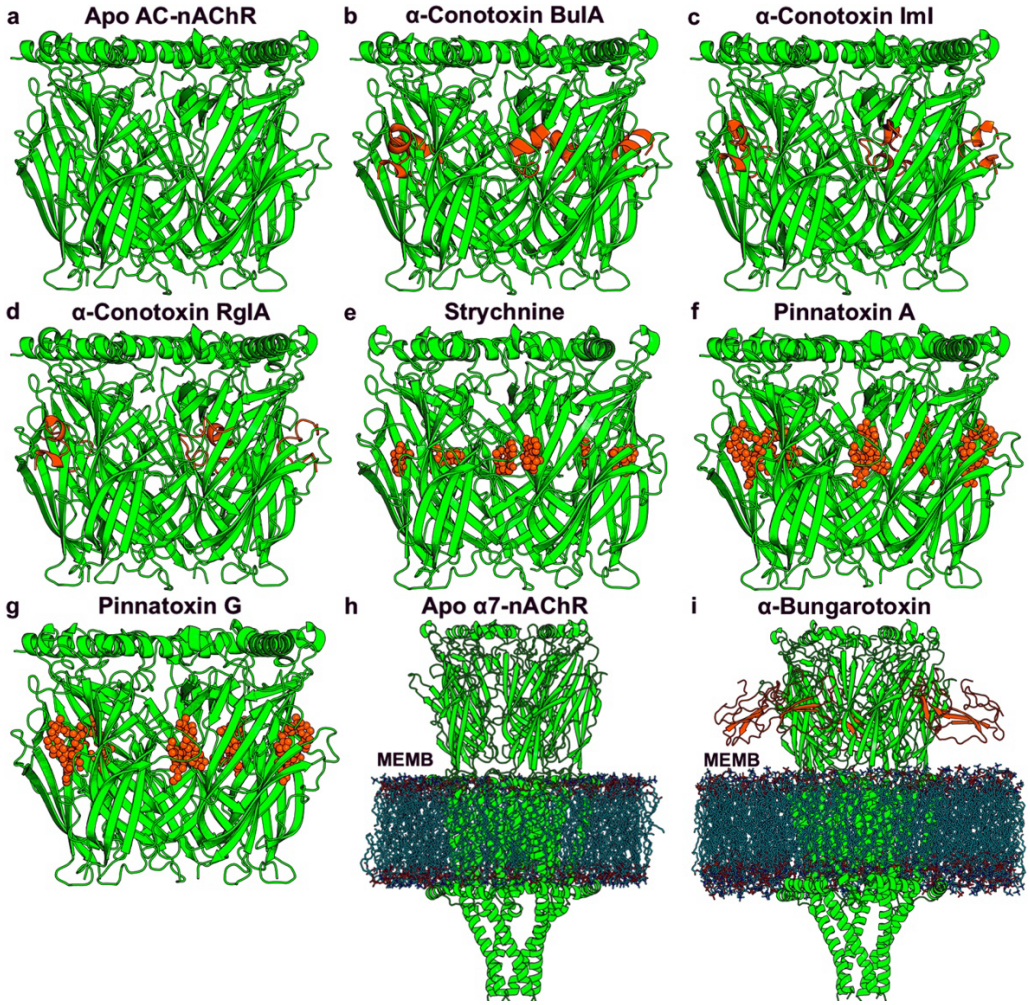

Figure 3. Dissociation of strychnine from the Aplysia californica nicotinic acetylcholine receptor. (a) Trace of the strychnine molecule dissociated from the nAChR observed in Sim4. A color scale of blue (0 ns) – white – red (1000 ns) is used to show the location of strychnine during Sim4. **(b)** 2D free energy profile of the strychnine dissociation from the nAChR calculated from the COM distance between strychnine and Cα atoms of the orthosteric binding pocket of nAChR (consisting of residues E:Q186 to E:Y195) and the pocket opening/closing distance (represented by the distance between the COM of the AC-nAChR orthosteric pocket and the COM of residues L29 to D44 and N48 to K61 from the neighboring subunit). Selected low-energy conformational states are labeled "S1"–"S4". **(c)** The "S1" state, where the distance between strychnine and nAChR orthosteric pocket is ~6.9 Å and the pocket opening/closing distance is ~20.2 Å. **(d)** The "S2" state, where the distance between strychnine and nAChR orthosteric pocket is ~9.8 Å and the pocket opening/closing distance is ~24.9 Å. **(e)** The "S3" state, where the distance between strychnine and nAChR orthosteric pocket is ~20.4 Å and the pocket opening/closing distance is ~25.2 Å. **(f)** The "S4" state, where the distance between strychnine and nAChR orthosteric pocket is ~36.2 Å and the pocket opening/closing distance is ~24.4 Å. The strychnine-1 is colored and circled in red, strychnine-2 is colored and circled in blue, while the nAChR orthosteric pocket of interest is colored cyan.

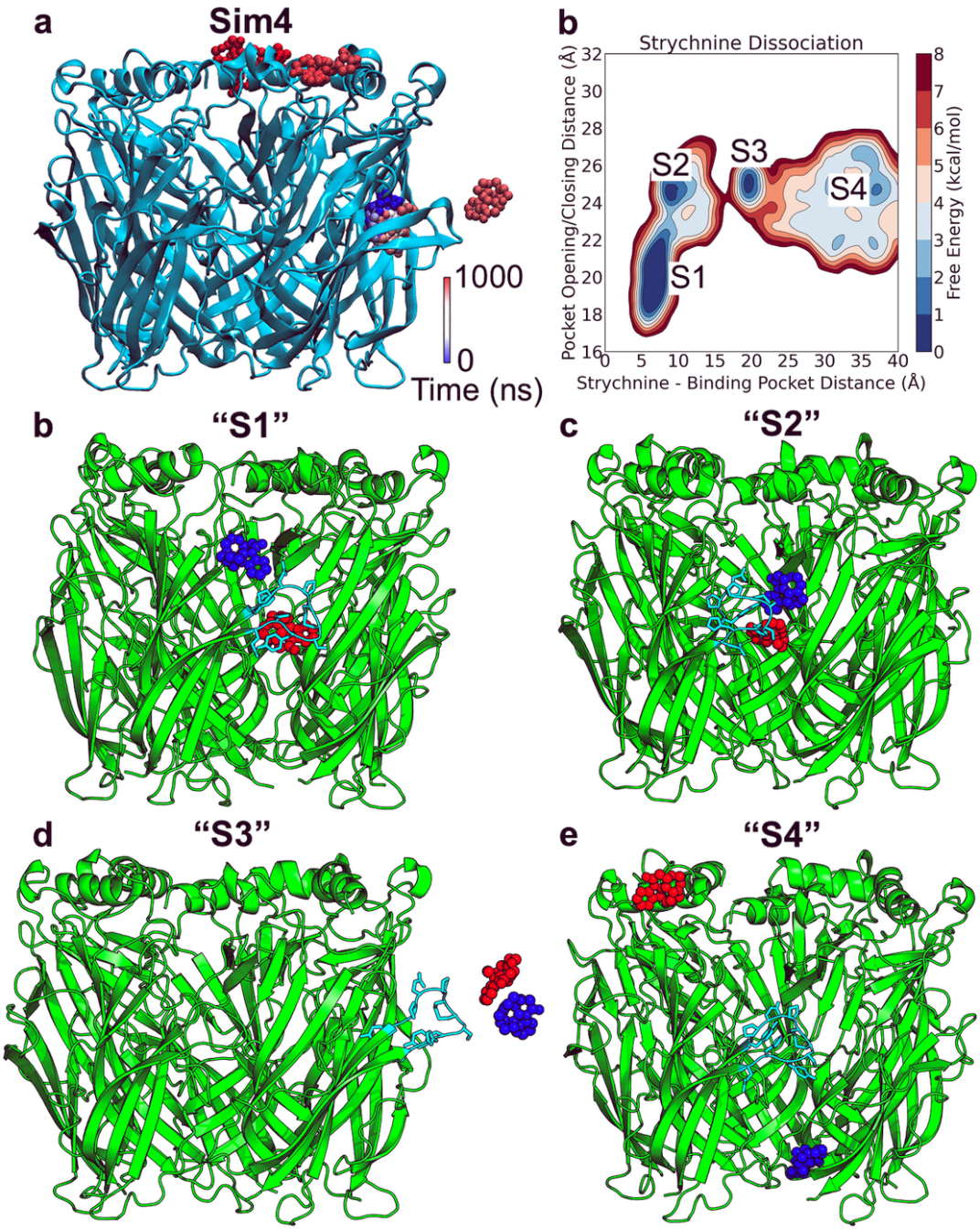
a
Sim4
1000
0
Time (ns)
b
Strychnine Dissociation
Pocket Opening/Closing Distance (Å)
Strychnine - Binding Pocket Distance (Å)
Free Energy (kcal/mol)
S1
S2
S3
S4
b
"S1"
c
"S2"
d
"S3"
e
"S4"

Figure 4. Binding of α-conotoxin RgIA to the Aplysia californica nicotinic acetylcholine receptor. (a) Representative trace of α-conotoxin RgIA binding to the AC nAChR observed in Sim2 within the last 500ns of the simulation. A color scale of blue (500 ns) – white – red (1000 ns) is used to show the location of α-conotoxin RgIA during Sim2. **(b)** 2D free energy profile of the α-conotoxin RgIA binding to the AC nAChR calculated from the COM distance between Cα atoms of RgIA and the orthosteric binding pockets of AC nAChR (consisting of residues Q186 – Y195 in the subunits) and the Cα-distance between residues A:Q100 and D:Q100. Selected low-energy conformational states are labeled "S1"–"S2". **(c)** The "S1" state, where the distance between RgIA and nAChR orthosteric pocket is ~9.1 Å and the nAChR pore diameter is ~20.8 Å. **(d)** The "S2" state, where the distance between RgIA and nAChR orthosteric pocket is ~19.8 Å and the nAChR pore diameter is ~20.7 Å. The α-conotoxin RgIA of interest is colored and red, while the nAChR orthosteric pocket of interest is colored cyan.

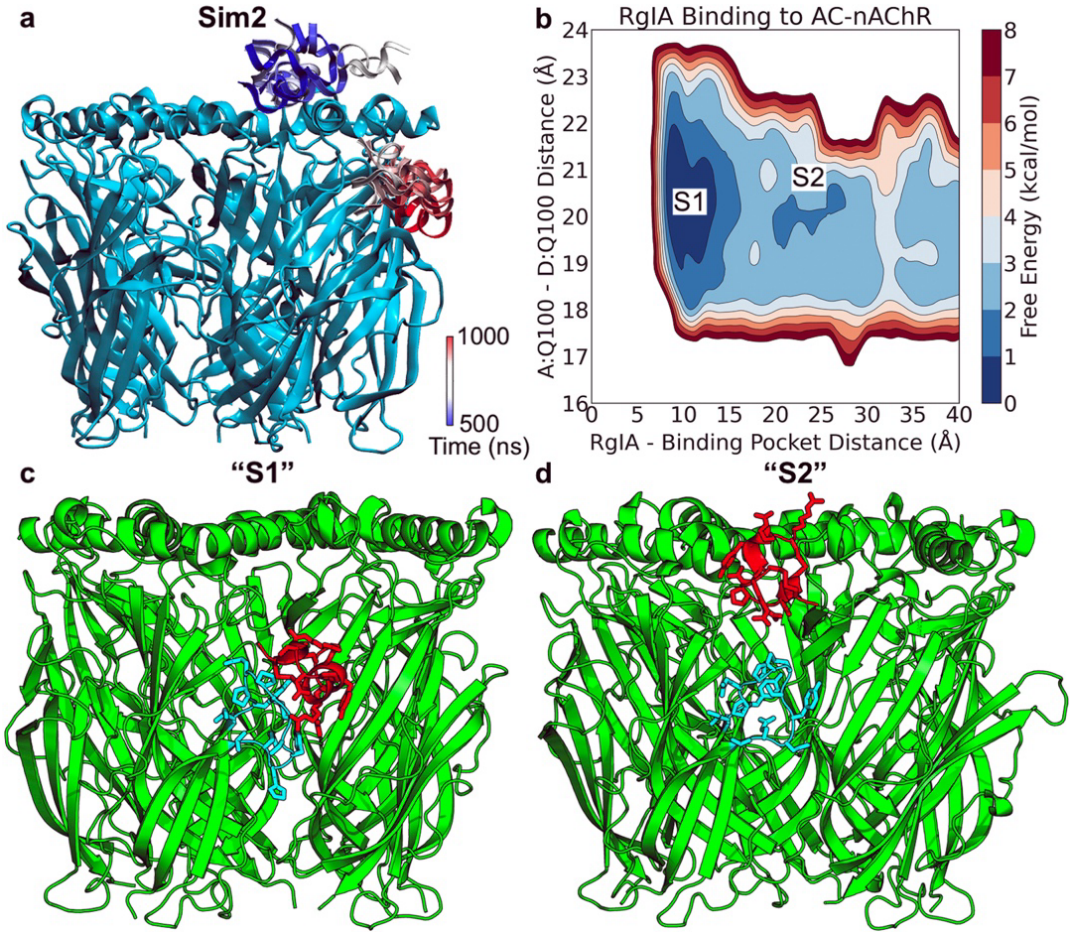

Figure 5. Electrostatic potential surfaces of the Aplysia californica (AC) nicotinic acetylcholine receptor (nAChR), **(b)** α-conotoxin BuIA that binds AC nAChR, **(c)** α-conotoxin ImI that binds AC nAChR, and **(d)** α-conotoxin RgIA that binds AC nAChR. Zoom-in views of the nAChR orthosteric pocket and α-conotoxins showed high complementarity in the electrostatic potentials between the nAChR orthosteric pocket and toxins **(a-d)**. The initial binding sites of the toxins at the outside of the nAChR extracellular pore (indicated by an arrow in **(a)**) could only accommodate the positive potential surface of the toxins. A color scheme of red (negative) – white – blue (positive) is used to show the electrostatic potential. The electrostatic potential surfaces of the human α7 nAChR and α-bungarotoxin were shown in **Figure S14**.

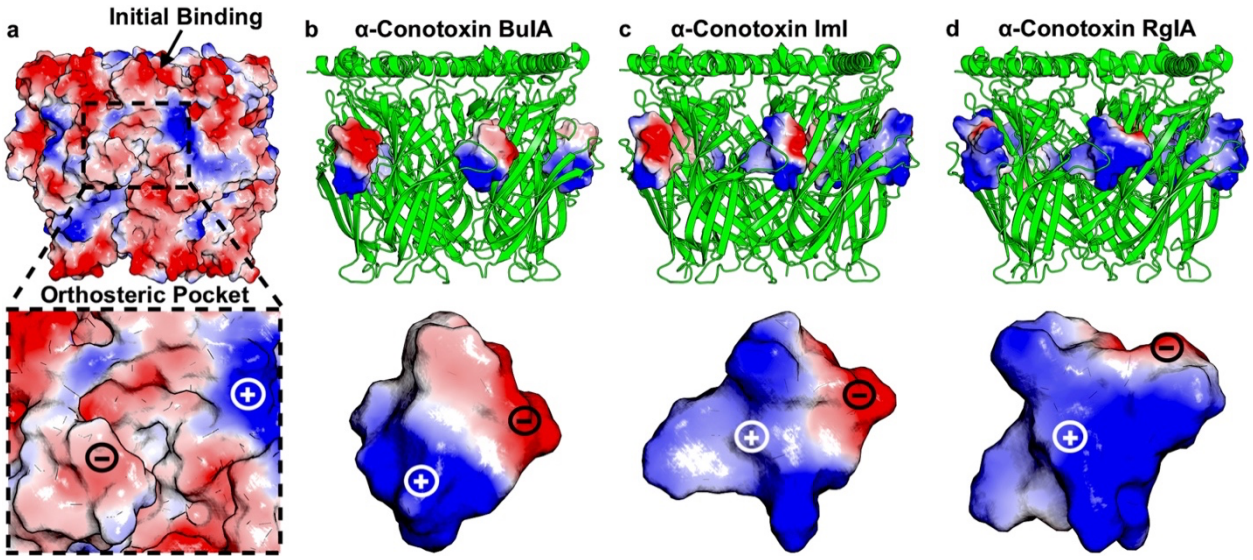

Table 1. Experimental binding affinities of the toxins towards the nAChRs explored in this study (Aplysia californica and α7) shown as ligand dissociation constants (K_d, nM). The binding affinity of the orthosteric ligand acetylcholine was included in the last row for reference purpose.

Toxin/Ligand	***AC-nAChR***	***α7-nAChR***
α-Conotoxin BulA	-*	-
α-Conotoxin ImI	0.88[50]	132[87]
α-Conotoxin RglA	-*	-
Strychnine	38.0 ± 3.3[16]	4,854 ± 133[16]
Pinnatoxin A	<0.05[17]	0.18 ± 0.1[17]
Pinnatoxin G	0.86 ± 0.09[17]	34 ± 4[17]
α-Bungarotoxin	-	0.1 ± 0.03[88]
Acetylcholine	30,000[89]	-

*Structural paper was unpublished.

Table 2. Summary of the MD simulations of toxin binding to the nicotinic acetylcholine receptors. Here, "AC" stands for the Aplysia californica organism. In the "Structural Domains" column, "LBD" indicates that the simulation system only includes the soluble extracellular ligand binding domain, whereas "Full" indicates that the simulation system includes the soluble extracellular ligand binding domain, membrane-bound transmembrane helices, and intracellular domains.

Simulation System	***Initial PDB***	***Structural Domains***	***Simulation Length***	***Boost Potential (kcal/mol)***
Apo AC-nAChR	2BYN[50]	LBD	5 x 1μs	12.1 ± 3.9
BuIA-bound AC-nAChR	4EZ1[34]	LBD	5 x 1μs	12.1 ± 3.9
ImI-bound AC-nAChR	2BYP[50]	LBD	5 x 1μs	13.1 ± 4.0
RgIA-bound AC-nAChR	7EGR[53]	LBD	5 x 1μs	12.5 ± 3.9
Strychnine-bound AC-nAChR	2XYS[16]	LBD	5 x 1μs	13.5 ± 4.1
PinnatoxinA-bound AC-nAChR	4XHE[17]	LBD	5 x 1μs	11.9 ± 3.8
PinnatoxinG-bound AC-nAChR	4XK9[17]	LBD	5 x 1μs	12.6 ± 3.9
AC-nAChR with free RgIA	7EGR[53]	LBD	5 x 1μs	11.8 ± 3.8
Apo human α7 nAChR	7EKI[90]	Full	5 x 1μs	13.9 ± 4.6
α-Bungarotoxin-bound α7 nAChR	7KOO[77]	Full	5 x 1μs	14.4 ± 4.6
α7 nAChR with free RgIA	7EKI[90]	Full	5 x 1μs	13.5 ± 4.3

Table 3. List of missing residues in the starting structures restored using the SWISS-MODEL homology modeling webserver[30].

Simulation System	*Initial PDB*	*Missing Residues*
Apo AC-nAChR	2BYN[50]	P18-M19
BuIA-bound AC-nAChR	4EZ1[34]	F14-M19
ImI-bound AC-nAChR	2BYP[50]	S17-M19

Table 4. Dipole moments (μ, Debyes) of the toxins and endogenous ligand (i.e., acetylcholine) of nAChR as calculated from their structures.

Toxin/Ligand	***μ (D)***
α-Conotoxin BulA	24.0
α-Conotoxin ImI	62.0
α-Conotoxin RgIA	153.4
Strychnine	4.7
Pinnatoxin A	13.7
Pinnatoxin G	3.0
α-Bungarotoxin	328.7
Acetylcholine	21.0
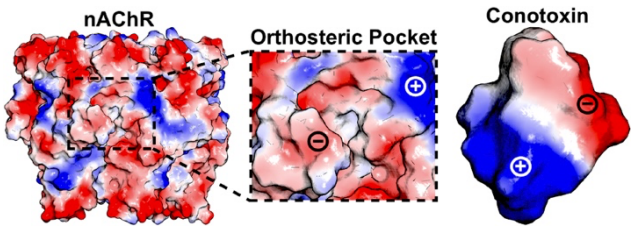
Table of Contents Graphic